

MoGe: Unlocking Accurate Monocular Geometry Estimation for Open-Domain Images with Optimal Training Supervision

Ruicheng Wang^{1*} Sicheng Xu² Cassie Dai^{3*} Jianfeng Xiang^{4*} Yu Deng² Xin Tong² Jiaolong Yang^{2†}
¹USTC ²Microsoft Research ³Harvard ⁴Tsinghua University

{t-ruiwang, sichengxu, t-jxiang, dengyu, jiaoyan}@microsoft.com {cccassied, xtong.gfx}@gmail.com



Figure 1. Given any image, our method reconstructs an affine-invariant 3D point map of the scene and can also produce a depth map and the camera focal length. The model yields high-quality shapes and generalizes well to open-domain images. (*Best view with zoom*)

*Work done during internship at Microsoft Research

†Corresponding author

Abstract

We present *MoGe*, a powerful model for recovering 3D geometry from monocular open-domain images. Given a single image, our model directly predicts a 3D point map of the captured scene with an affine-invariant representation, which is agnostic to true global scale and shift. This new representation precludes ambiguous supervision in training and facilitate effective geometry learning. Furthermore, we propose a set of novel global and local geometry supervisions that empower the model to learn high-quality geometry. These include a robust, optimal, and efficient point cloud alignment solver for accurate global shape learning, and a multi-scale local geometry loss promoting precise local geometry supervision. We train our model on a large, mixed dataset and demonstrate its strong generalizability and high accuracy. In our comprehensive evaluation on diverse unseen datasets, our model significantly outperforms state-of-the-art methods across all tasks, including monocular estimation of 3D point map, depth map, and camera field of view. Code and models will be released on our [project page](#).

1. Introduction

Estimating the 3D geometry of general scenes is a fundamental task in computer vision. While 3D reconstruction from a set of images has been extensively studied with Structure-from-Motion (SfM) [1, 47] and Multi-View Stereo (MVS) [48, 64] techniques, recovering the 3D geometry from a single image in an arbitrary domain remains a significant challenge due to its highly ill-posed nature.

For monocular geometry estimation (MGE), a common approach involves first estimating a depth map, subject to an unknown scale (and shift), and then combining it with camera intrinsics to recover the 3D shape via unprojection [41, 69]. For the former, significant advancements in monocular depth estimation (MDE) have been achieved in recent years by training on large-scale data [20, 29, 65, 71]. However, inferring camera intrinsics (e.g., focal length) from single images remains challenging due to the high degree of ambiguity when strong geometric cues are absent. Inaccurate camera parameters can lead to significant geometry distortions even when used with ground truth depth maps. Recently, DUS3R [57] proposed predicting a 3D point map from an image by mapping each pixel to a free 3D point, thereby bypassing camera parameter estimation during geometry recovery. Although the model can estimate monocular geometry, it is primarily designed for multi-view scenarios and is trained on image pair inputs.

In this paper, we introduce a new *direct* 3D geometry estimation method designed for single images in the open domain. Our model architecture is simple and straightforward:

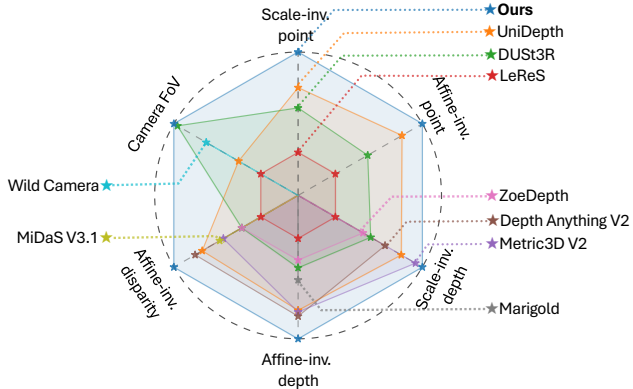


Figure 2. Accuracy ranking of existing methods and ours in our extensive evaluation on monocular 3D point map (scale-invariant and affine-invariant), depth map (scale-invariant depth, affine-invariant depth, and affine-invariant disparity), and camera field of view. Outer methods rank higher. See our experiments for details.

it directly predicts point maps from images, which can further derive depth map and camera focal length or FOV if needed. Different from DUS3R [57] which uses scale-invariant point maps, our method predicts *affine-invariant* point maps, where the 3D points are subject to an unknown global scale as well as a 3D shift. This alteration is important as it eliminates the focal-distance ambiguity which is detrimental to the network training – we provide intuitive explanations with illustration as well as empirical evidence to support this advancement.

More importantly, our findings indicate that *the design of training supervisions is crucial* to achieve robust and accurate point map prediction from single images. Similar to previous MDE approaches, we need to compute a global scaling factor and a translation to align the predicted results with the ground truth during training. However, previous methods for this global alignment calculation are either sensitive to outliers or solved with coarse approximations, leading to unsatisfactory supervision. We propose a *Robust, Optimal, and Efficient (ROE)* global alignment solver to resolve scale and shift for the affine-invariant pointmap loss, which substantially improved the training effectiveness and final accuracy. On the other hand, the effective learning of local, region-wise geometry has been largely neglected previously. In monocular geometry estimation, the relative distance between different objects can be ambiguous, which hinders precise local geometry learning when a global alignment computed with all objects is applied. In light of this, we propose a *multi-scale local geometry loss*, which imposes penalties on the local discrepancies of 3D point clouds, each under independent and optimal affine alignment. This design significantly boosted the accuracy of our local geometry prediction.

We train our model on a large-scale training corpus

sourced from various existing datasets. Our model demonstrates strong generalizability and accuracy in monocular geometry estimation for open-domain images (some examples are shown in Fig. 1). The zero-shot evaluation on eight unseen datasets shows that it outperforms previous MGE methods that output point clouds by a large margin (over **35%** error reduction compared to the previous best). Moreover, our method also significantly outperforms previous approaches that focus on the sub-tasks of MDE and camera FoV (**20%~30%** error reduction for the former and over **20%** for the latter). Figure 2 shows the performance ranking of different methods in our evaluation, where our method ranks top across all tasks/metrics and among all compared methods.

Our contributions are summarized as follows: 1) We propose a new direct MGE method for open-domain images using affine-invariant point maps. 2) We establish a set of novel and effective global and local supervisions for robust and precise geometry recovery. 3) We demonstrate the substantial enhancement in performance of our model over existing methods on MGE, MDE, and camera FOV estimation across diverse datasets. We hope that our method can serve as a strong and versatile foundational model for solving monocular geometry problems, facilitating applications such as 3D-aware image editing, image relighting, depth-to-image synthesis, novel view synthesis, and 3D scene understanding, as well as providing initial geometrical priors for video-based or multiview-based 3D reconstruction.

2. Related Work

Monocular depth estimation. As a crucial precursor to monocular geometry estimation, monocular depth estimation is a long-standing task and has been extensively studied in the past. A number of methods [4, 5, 18, 26, 35, 41, 71] have been developed to estimate depth with metric scale, which often rely heavily on data from specific sensors such as RGBD cameras, LiDAR, and calibrated stereo cameras. This dependence restricts their applicability to specific domains, such as indoor and driving scenes. In contrast, relative depth estimation has garnered significant attention due to its ability to utilize a much wider variety of data, thereby exhibiting enhanced generalizability. A prevalent approach is to predict relative depth in an affine-invariant manner, either through direct regression [10, 11, 22, 34, 42, 65, 66, 68] or generative modeling [20, 23, 29, 54]. Despite the recent advancements in monocular depth estimation, recovering 3D shape from depth information always necessitates known camera intrinsics.

Monocular point map estimation. Compared to depth map, 3D point map offers a more straightforward representation of 3D geometry. Monocular point map estimation aims to recover free 3D points for each pixel on a single im-

age. Several approaches tackle this challenge by predicting camera parameters alongside depth estimation. For example, LeReS [69, 70] introduced a two-stage pipeline with an affine-invariant depth prediction module followed by a point cloud module for recovering shift and camera focal length. UniDepth [41] proposed a self-promptable camera module that predicts dense camera representation to condition the subsequent depth estimation module. DUS_t3R [57] employs a more straightforward end-to-end model to directly map two-view images to camera space point maps, and it can adapt to monocular scenarios by using two identical images as input. It uses the camera-space scale-invariant pointmap which incorporates camera shift information. This representation can suffer from the focal-distance ambiguity and jeopardize pointmap learning. In contrast, our approach is designed to handle monocular input and we employ affine-invariant point map with meticulously designed training supervisions for more effective geometry learning.

Camera intrinsics estimation. Estimating camera intrinsics is a fundamental task in 3D vision. While traditional multiview camera calibration using special patterns is well studied [73], estimating camera intrinsics from single images is ill-posed and remains challenging. For the latter, earlier works utilized known 3D shapes [59] or vanishing points [13] to solve the problem. More recently, learning-based approaches have been proposed [7, 28, 32, 61, 75] to handle in-the-wild images, but the results are far from satisfactory. In this work, we demonstrate that our camera parameter estimation derived from point maps can achieve state-of-the-art accuracy and offer remarkable generalizability.

Large-scale data training for monocular geometry. Recently, there has been an emerging trend [5, 17, 26, 41, 42, 57, 65, 66, 71] in monocular geometry estimation and depth estimation that leverages large-scale datasets coupled with advanced network backbones [15, 40, 43] to enhance performance. MiDaS [42] marks an important milestone by mixing large datasets from various domains for training. Depth Anything [65] leverages both labeled and extensive unlabeled data to improve generalization. Its successive work [66] further highlights the importance of high-quality synthetic data for capturing rich shape details in depth prediction. These advancements underscore the vital importance of large-scale training data in improving the performance of monocular geometry estimation.

3. Approach

Our method takes a single image as input and directly predicts the geometry of the scene represented by 3D points. An overview of the method is shown in Fig. 3.

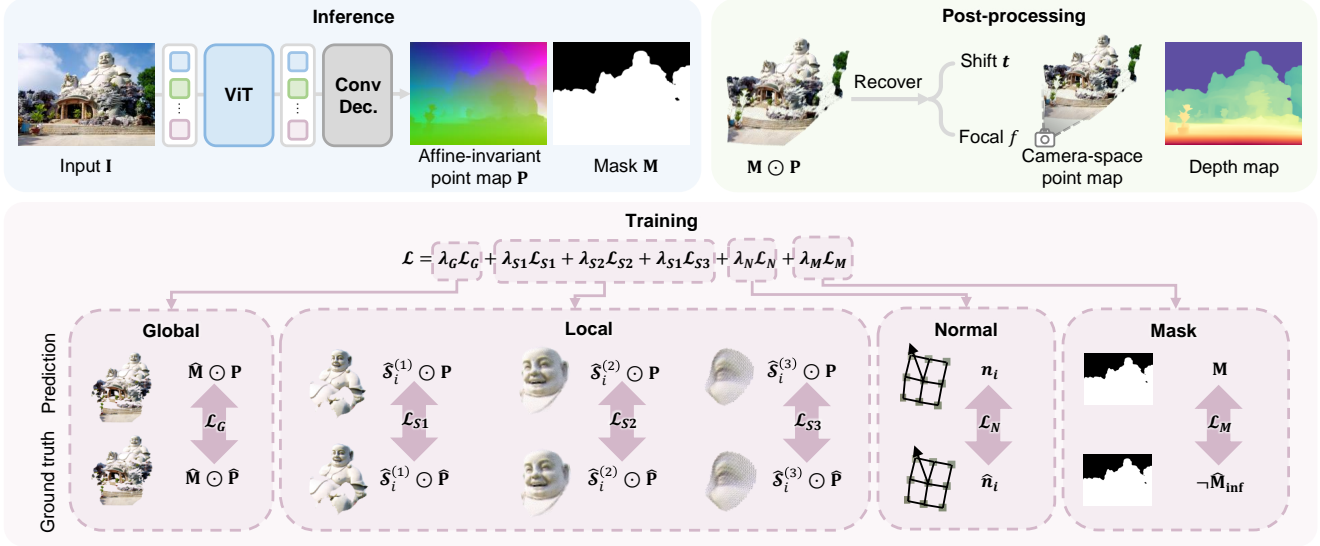


Figure 3. Method overview. Our model consists of a ViT encoder and a convolutional decoder. It predicts an affine-invariant point map as well as a mask that excludes regions with undefined geometry (e.g., infinity). Depth, camera shift, and focal length can be further derived from the model output. For training, we design robust and effective supervisions focusing on both the global and local geometry.

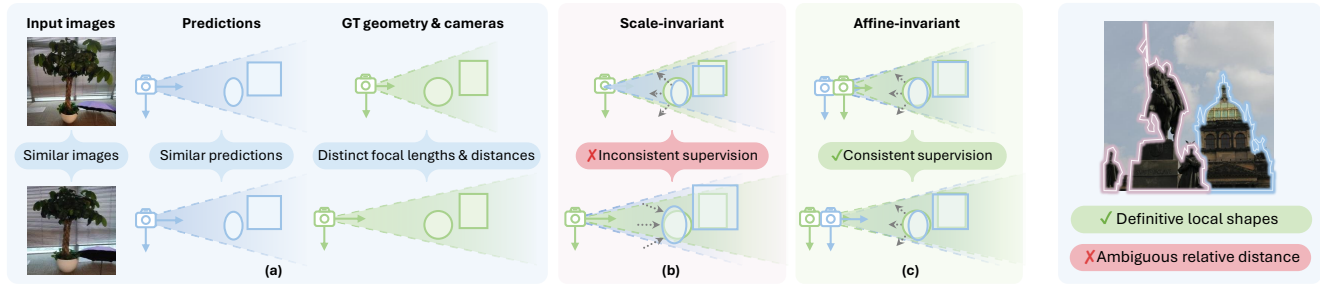


Figure 4. The focal-distance ambiguity and effects of different 3D point representations. (a) For similar images captured with varying camera focal length and distance to the objects, perceiving their true camera setup is challenging and models often produce similar geometries. (b) Inconsistent supervision signals occur with only scale alignment. (c) Consistent geometry supervision with an additional translation alignment.

Figure 5. The relative distance ambiguity, where distances between objects can be hard to predict.

3.1. Affine-invariant point map

For an image $\mathbf{I} \in \mathbb{R}^{H \times W \times 3}$, our model F_θ infers the 3D coordinates of the image pixels, represented by a point map $\mathbf{P} \in \mathbb{R}^{H \times W \times 3}$, i.e.,:

$$F_\theta : \mathbf{I} \mapsto \mathbf{P}. \quad (1)$$

The X and Y axes of the coordinate frame of \mathbf{P} are aligned with the u and v axes in the image space respectively.

Monocular geometry estimation often suffers from focal-distance ambiguity, as shown in Fig. 4 (a). To deal with this issue, we propose to predict *affine-invariant* point map \mathbf{P} , i.e., \mathbf{P} is agnostic to the global scale $s \in \mathbb{R}$ and offset $\mathbf{t} \in \mathbb{R}^3$ and thus $\mathbf{P} \cong s\mathbf{P} + \mathbf{t}, \forall s, \forall \mathbf{t}$. Compared to the scale-invariant supervision [57] shown in Fig. 4 (b), the discrepancies in focal lengths and camera positions between the predictions and ground truth are amended by a transla-

tion, as shown in Fig. 4 (c). This ensures consistent geometry supervision when focal length is ambiguous, enabling more effective geometry learning.

Following accepted practice, we assume that the camera principal point coincides with image center and pixels are square. In this case, \mathbf{t} can be simplified with a Z -axis shift t_z (i.e., $t_x = t_y = 0$).

Recovering camera focal and shift. The affine-invariant point map representation can be used to recover both camera shift and focal length. Given the predicted 3D points (x_i, y_i, z_i) and their corresponding 2D pixels (u_i, v_i) , we solve for camera focal length f and Z -axis shift by minimizing the projection error:

$$\min_{f, t'_z} \sum_{i=1}^N \left(\frac{fx_i}{z_i + t'_z} - u_i \right)^2 + \left(\frac{fy_i}{z_i + t'_z} - v_i \right)^2, \quad (2)$$

where $t'_z = t_z/s$. Eq. 2 can be efficiently solved with a fast iterative optimization algorithm, which converges within 10 iterations, taking approximately 3ms. More details about the solution can be found in the *suppl. materials*.

With t'_z recovered, the scale-invariant depth map and point map in the camera space can be obtained by adding it to the z coordinates.

3.2. Training Objectives

Global point map supervision. Let $\hat{\mathbf{p}}_i$ denote the predicted 3D point for the i -th pixel, and \mathbf{p}_i the corresponding ground truth. The global point map loss is defined as:

$$\mathcal{L}_G = \sum_{i \in \mathcal{M}} \frac{1}{z_i} \|s\hat{\mathbf{p}}_i + \mathbf{t}^* - \mathbf{p}_i\|_1, \quad (3)$$

where $\|\cdot\|_1$ denotes the L_1 norm, s and \mathbf{t} are the alignment parameters that transform the predicted affine-invariant point map to the ground-truth camera space, and \mathcal{M} is the mask for regions with labels. The weighting term $\frac{1}{z_i}$, where z_i is the z -coordinate of \mathbf{p}_i , is applied to balance the supervision signal across extreme depths variations.

To apply the global loss \mathcal{L}_G for training, we need to first determine s and \mathbf{t} . Previous methods for affine-invariant depth estimation often use coarse approximations for this alignment. For example, a predominate strategy is to use the median depth values of the two sets as the anchor to compute shift followed by scaling factor calculation [42, 65, 66]. The range normalization strategy used by [20, 29] can be viewed as computing shift using minimal or a predefined fraction of depth values. All these simple strategies are non-optimal for the problem setup and could lead to unsatisfactory supervision.

In this work, we propose an *optimal* solver to the alignment parameters. Specifically, we determine s^* and \mathbf{t}^* via

$$(s^*, \mathbf{t}^*) = \operatorname{argmin}_{s, \mathbf{t}} \sum_{i \in \mathcal{M}} \frac{1}{z_i} \|s\hat{\mathbf{p}}_i + \mathbf{t} - \mathbf{p}_i\|_1, \quad (4)$$

where t_x and t_y are 0. One possible approach to solve this equation is to formulate it as an absolute residuals optimization problem and solve it using linear programming techniques such as simplex algorithms and the interior-point method [8]. However, these methods are known to have high computational complexity, often exceeding $O(N^3)$. Given thousands of points, a typical implementation may require computation time of a few seconds or even higher, which is inefficient for network training.

Instead, we develop an efficient *parallelized searching algorithm* to solve it optimally. Our theoretical analysis (Sec. A.2) demonstrates that the minimum must occur when $s\hat{z}^{(k)} + t_z - z^{(k)} = 0$ for some $k = 1, \dots, N$, $k \in \mathcal{M}$. This insight allows us to substitute t_z with s and decompose the problem into a series of one-dimensional subproblems with

Algorithm 1 Optimal alignment solver to Eq. 4

function SOLVE.SUBPROBLEM

Enumerating non-differentiable points of objective function, at zero per-coordinate alignment residuals.

Determining extrema by derivative computation.

Return $s^{(k)}$ with smallest objective value $l^{(k)}$ at extrema.

end function

for index $k = 1, \dots, N$ **do** \triangleright parallel computation

Formulate subproblem by substituting t_z with $z^{(k)} - s\hat{z}^{(k)}$.

Solve scale $s^{(k)}$ and $l^{(k)}$ via SOLVE.SUBPROBLEM.

Obtain translation $t_z^{(k)}$ as $z^{(k)} - s^{(k)}\hat{z}^{(k)}$.

end for

Select optimal s^* and t_z^* with smallest function value $l^{(k)}$.

scale variable only, which can be solved in parallel. The overall computational complexity is $O(N^2 \log N)$ and efficient training is achieved on GPU. A high-level description of this solution is presented in Algorithm 1 and more details can be found in the *suppl. materials*.

In practice, we noticed that Eq. 4 is still sensitive to outliers even if the L_1 error norm has been used. If the model wrongly predicts a close foreground edge pixel as a far background point, the objective will be dominated by the incorrect edge prediction. To further improve the robustness, we apply a clipping operator $\operatorname{clip}(\cdot, \tau) = \max(\min(\cdot, \tau), -\tau)$ on the per-point residuals, which brings accuracy gains as we will show in the experiments. Adding the clipping operator makes the problem non-convex, but our optimal solver is still applicable with minor modifications.

In summary, our alignment solver is made *Robust*, *Optimal*, and *Efficient*, and hence we call it the *ROE* solver.

Multi-scale local geometry loss. In monocular geometry estimation, the relative distance between different objects can be ambiguous and difficult to predict, as illustrated in Fig. 5. This hinders precise local geometry learning when a global alignment computed with all objects is applied. To enhance the supervision for local geometry, we propose a loss function which measures the accuracy of local sphere regions with *independent* alignment.

Specifically, given a ground-truth 3D point \mathbf{p}_j as the anchor, we first select the point set within the spherical region centered at \mathbf{p}_j , defined as:

$$\mathcal{S}_j = \{i \mid \|\mathbf{p}_i - \mathbf{p}_j\| \leq r_j, i \in \mathcal{M}\}, \quad (5)$$

where r_j is the radius. We set $r_j = \alpha \cdot z_j \cdot \frac{\sqrt{W^2 + H^2}}{2 \cdot f}$ where z_j is the z -coordinate of \mathbf{p}_j , f is the focal length, and W and H are image width and height. This way, the hyper-parameter $\alpha \in (0, 1)$ approximates the proportion of the projected sphere’s diameter to the image diagonal.

Then, we apply the aforementioned ROE alignment solver to align the point maps and compute error. For each

sphere scale parameter α , we sample a set of anchor points \mathcal{H}_α and compute the loss as

$$\mathcal{L}_{S(\alpha)} = \sum_{j \in \mathcal{H}_\alpha} l_{S_j} = \sum_{j \in \mathcal{H}_\alpha} \sum_{i \in S_i} \frac{1}{z_i} \|s^* \hat{\mathbf{p}}_i + \mathbf{t}^* - \mathbf{p}_i\|_1 \quad (6)$$

In practice, we use three α scales ranging from coarse to fine: 1/4, 1/16, and 1/64, denoted as \mathcal{L}_{S_1} , \mathcal{L}_{S_2} and \mathcal{L}_{S_3} , respectively.

Normal loss. For better surface quality, we additionally supervise the normal computed from the predicted point map with the ground truth:

$$\mathcal{L}_N = \sum_{i \in \mathcal{M}} \angle(\hat{\mathbf{n}}_i, \mathbf{n}_i) \quad (7)$$

where the normal \mathbf{n}_i of pixel i is obtained from the cross product of its adjacent edges on the image grid.

Mask loss. The distance to infinity region (*e.g.*, sky) in outdoor scenes and plain backgrounds in object-only images are undefined. We add a single-channel head to our model for predicting the mask $\hat{\mathbf{M}} \in \mathbb{R}^{H \times W}$ where the distance is valid:

$$\mathcal{L}_M = \|\hat{\mathbf{M}} - (1 - \mathbf{M}_{\text{inf}})\|_2^2 \quad (8)$$

where \mathbf{M}_{inf} is the infinity mask label. For synthetic data, the ground truth masks are readily available, while for real outdoor scenes, we use SegFormer [62] to obtain sky masks.

At inference time, we use a threshold of 0.5 to binarize the mask prediction. Recovery camera focal and shift involves masked points only, excluding the regions of meaningless geometry.

3.3. Training data

Recently, numerous synthetic and real RGBD datasets have been utilized in large-scale training for monocular geometry estimation. In this work, we collected 21 datasets from various domains to train our model. The total number of collected frames is around 9 million. Details of these datasets and their mixing ratios can be found in the *suppl. materials*.

Since the quality of data labels are varied, we apply different loss function combinations tailored for different data sources. As shown in Table 1, higher quality and less noisy data are assigned with finer-level loss functions. To address imperfections and potential outliers in real labels, we exclude the top 5% of per-pixel loss values for real data. Following DINOv2 [40], we rebalance the collected datasets using image retrieval from a curated image set to address uneven or biased data distributions. See the *suppl. materials* for details.

Table 1. Label quality and applied losses for different training sources.

Source	Label quality			Applied losses					
	Accuracy	Range	Density	\mathcal{L}_G	\mathcal{L}_{S_1}	\mathcal{L}_{S_2}	\mathcal{L}_{S_3}	\mathcal{L}_N	\mathcal{L}_M
Synthetic	Perfect	∞	Dense	✓	✓	✓	✓	✓	✓
SfM/MV Recon	High	∞	Dense&Partial	✓	✓	✓			✓
LiDAR/Laser	High	$\sim 100\text{m}$	Sparse	✓	✓				✓
Kinect	Medium	$\sim 10\text{m}$	Dense	✓					✓

4. Experiments

Implementation details. We employ a ViT [15] encoder and a light-weight CNN-based upsampler as the decoder. The encoder is pretrained with DINOv2 [40]. The initial learning rates for the encoder and decoder are set to 5×10^{-6} and 5×10^{-5} , with a decay factor of 5 applied for every 100K iterations. The training batch size is 256. Our model is trained on images with varying aspect ratio and resolutions, where aspect ratios are uniformly sampled between 1 : 2 and 2 : 1, and pixel counts range from 250K to 500K. We apply several image augmentations, including color jittering, Gaussian blurring, JPEG compression-decompression, and random cropping. The principal point of the cropped image is aligned with its center using a perspective crop.

4.1. Quantitative Evaluations

We assess the zero-shot performance of our model and compare it with several state-of-the-art methods for monocular point map estimation [41, 57, 69] and depth map estimation [5, 6, 20, 26, 29, 65, 66]. To ensure a fair comparison, all methods utilize ViT-Large [15] as backbone, except for LeReS (which employs ResNeXt101 [63]) as well as GeoWizard and Marigold (both use StableDiffusion V1 [45]). For a valid evaluation, the scale and shift of the predicted point maps and depth maps are first aligned with the ground truth when necessary. We also evaluate the FoV prediction results against several recent methods [28, 75]. As detailed below, *our method achieves superior results across all evaluation metrics for various tasks on different benchmarks*.

Point map estimation. We evaluate the accuracy of point map estimation on eight diverse datasets: NYUv2 [38], KITTI [51], ETH3D [49], iBims-1 [31], Sintel [9], Google Scanned Objects (GSO) [16], DDAD [24], and DIODE [52]. These datasets represent a wide range of domains, including indoor scenes, street views, object scans, and synthetic movies. The raw datasets are processed for reliable evaluation (*e.g.*, sky regions in Sintel dataset and boundary artifacts in the DIODE are removed; see the *suppl. material* for more preprocessing details). For evaluation metrics, we use the relative point error Rel^p , *i.e.*, $\|\mathbf{p} - \hat{\mathbf{p}}\|_2 / \|\hat{\mathbf{p}}\|_2$, and the percentage of inliers δ_1^p with $\|\mathbf{p} - \hat{\mathbf{p}}\|_2 / \|\hat{\mathbf{p}}\|_2 < 0.25$.

We evaluate our method and compare it with LeReS [69],

Method	NYUv2		KITTI		ETH3D		iBims-1		GSO		Sintel		DDAD		DIODE		Average		
	Rel ^P _↓	δ ₁ ^P _↑	Rel ^P _↓	δ ₁ ^P _↑	Rel ^P _↓	δ ₁ ^P _↑	Rel ^P _↓	δ ₁ ^P _↑	Rel ^P _↓	δ ₁ ^P _↑	Rel ^P _↓	δ ₁ ^P _↑	Rel ^P _↓	δ ₁ ^P _↑	Rel ^P _↓	δ ₁ ^P _↑	Rel ^P _↓	δ ₁ ^P _↑	Rank _↓
Scale-invariant point map																			
LeReS	17.0	76.0	37.3	11.1	17.1	75.8	18.5	72.1	14.7	75.9	38.6	30.6	31.9	39.6	27.5	46.7	25.3	53.5	3.94
DUST3R	5.56	97.1	21.9	63.6	<u>10.7</u>	<u>90.5</u>	6.17	95.4	<u>4.55</u>	99.3	34.8	<u>50.4</u>	21.3	70.3	<u>12.3</u>	87.0	14.7	81.7	2.69
UniDepth	<u>5.36</u>	98.3	<u>10.7</u>	98.0	18.5	77.5	<u>5.27</u>	<u>97.4</u>	6.57	<u>99.6</u>	<u>33.0</u>	49.0	11.3	<u>90.3</u>	12.3	<u>91.1</u>	<u>12.9</u>	<u>87.7</u>	<u>2.18</u>
Ours	4.91	98.4	8.62	<u>96.3</u>	4.60	98.9	4.62	97.1	2.60	100	22.3	69.4	<u>12.3</u>	90.4	6.50	94.7	8.32	93.1	1.12
Affine-invariant point map																			
LeReS	9.55	91.4	29.0	43.8	14.7	79.6	11.0	88.7	8.89	95.3	29.7	55.5	29.3	46.8	14.9	80.3	18.4	72.7	3.94
DUST3R	4.49	97.4	18.0	66.7	<u>7.27</u>	<u>94.9</u>	5.02	96.0	3.08	99.5	30.3	56.7	19.6	71.4	8.86	88.9	12.1	83.9	2.94
UniDepth	<u>3.96</u>	98.4	<u>7.94</u>	97.3	12.2	89.6	<u>4.62</u>	98.0	<u>2.98</u>	<u>99.8</u>	<u>28.5</u>	<u>58.5</u>	10.2	<u>90.6</u>	<u>8.46</u>	<u>91.1</u>	<u>9.86</u>	<u>90.4</u>	<u>1.88</u>
Ours	3.73	<u>98.3</u>	7.69	<u>95.0</u>	3.60	99.0	3.60	<u>97.3</u>	1.16	100	16.9	77.8	<u>10.4</u>	91.5	4.31	96.6	6.43	94.4	1.25
Local point map																			
LeReS	-	-	-	-	8.62	91.5	15.7	84.4	-	-	18.7	85.8	1.65	99.0	16.2	85.2	12.2	89.2	3.70
DUST3R	-	-	-	-	<u>5.88</u>	<u>94.4</u>	<u>9.43</u>	<u>91.3</u>	-	-	<u>12.7</u>	<u>88.3</u>	1.71	98.9	<u>10.1</u>	<u>91.3</u>	7.96	92.9	2.30
UniDepth	-	-	-	-	7.45	92.7	10.2	90.2	-	-	17.0	86.9	<u>1.64</u>	98.8	13.2	87.8	9.89	91.3	3.00
Ours	-	-	-	-	2.86	97.9	7.02	94.1	-	-	9.73	92.1	1.08	99.5	5.96	95.2	5.33	95.8	1.00

Table 2. Quantitative results for point map estimation. Rel^P and δ₁^P are in percentage. The best values are highlighted in **bold**, and the second-best ones are underlined. Local point map accuracy is evaluated on affine-invariant point maps within local object regions.

Method	NYUv2		KITTI		ETH3D		iBims-1		GSO		Sintel		DDAD		DIODE		Average		
	Rel ^d _↓	δ ₁ ^d _↑	Rel ^d _↓	δ ₁ ^d _↑	Rel ^d _↓	δ ₁ ^d _↑	Rel ^d _↓	δ ₁ ^d _↑	Rel ^d _↓	δ ₁ ^d _↑	Rel ^d _↓	δ ₁ ^d _↑	Rel ^d _↓	δ ₁ ^d _↑	Rel ^d _↓	δ ₁ ^d _↑	Rel ^d _↓	δ ₁ ^d _↑	Rank _↓
Scale-invariant depth																			
LeReS	12.1	82.5	19.3	64.3	14.2	78.4	14.0	78.8	13.6	77.9	30.5	52.1	26.5	52.1	18.1	69.9	18.5	69.5	7.31
ZoeDepth	5.65	96.3	7.23	92.2	10.4	87.3	7.48	93.2	3.23	99.9	27.4	61.7	17.0	73.0	11.2	85.4	11.2	86.1	5.50
DUST3R	4.43	97.1	7.71	90.9	6.07	95.6	4.96	95.9	3.27	99.5	31.1	57.2	18.5	73.5	8.84	88.8	10.6	87.3	5.00
Metric3D V2	4.74	97.3	<u>3.96</u>	<u>98.6</u>	<u>3.92</u>	<u>98.5</u>	<u>4.20</u>	<u>97.7</u>	<u>2.47</u>	<u>99.9</u>	<u>20.7</u>	<u>70.0</u>	<u>7.36</u>	<u>94.6</u>	3.27	98.5	<u>6.32</u>	<u>94.4</u>	<u>2.07</u>
UniDepth	<u>3.88</u>	98.3	3.73	98.7	5.68	97.0	4.76	97.4	4.17	99.7	28.3	58.9	<u>9.98</u>	<u>90.7</u>	6.79	92.9	<u>8.41</u>	<u>91.7</u>	3.00
DA V1	4.81	97.5	<u>5.52</u>	<u>95.8</u>	8.80	92.3	5.54	95.8	5.48	99.2	28.1	56.7	13.1	81.7	10.1	87.8	10.2	88.4	5.67
DA V2	5.09	97.2	7.28	93.6	6.14	95.5	4.33	97.9	4.40	99.3	22.9	65.3	14.6	78.2	7.89	90.3	9.08	89.7	4.06
Ours	3.48	98.4	4.27	97.8	3.38	98.9	3.45	97.1	1.49	100	19.4	73.4	9.11	90.6	<u>4.85</u>	<u>94.8</u>	6.17	93.9	1.62
Affine-invariant depth																			
Marigold	<u>4.63</u>	97.3	<u>7.29</u>	<u>93.8</u>	<u>6.08</u>	<u>96.3</u>	<u>4.35</u>	<u>97.2</u>	2.78	99.9	21.2	75.0	<u>14.6</u>	<u>80.5</u>	<u>6.34</u>	<u>94.3</u>	<u>8.41</u>	<u>91.8</u>	<u>2.25</u>
GeoWizard	4.69	97.4	8.14	92.5	6.90	94.0	4.50	97.1	<u>2.00</u>	<u>99.9</u>	<u>17.8</u>	<u>76.2</u>	16.5	75.7	7.03	92.7	8.44	90.7	2.69
Ours	2.97	98.6	3.95	98.0	2.71	99.2	2.73	97.9	0.96	100	13.1	83.1	8.33	92.2	3.13	97.6	4.73	95.8	1.56
Affine-invariant disparity																			
MiDaS V3.1	4.62	98.1	6.30	94.8	5.80	96.8	4.75	97.4	1.88	100	21.4	73.0	14.4	82.7	6.06	94.9	8.15	92.2	3.69
DA V1	4.24	98.4	<u>5.40</u>	<u>97.0</u>	<u>4.70</u>	<u>98.2</u>	4.20	97.6	1.54	100	<u>20.4</u>	<u>77.5</u>	<u>12.6</u>	<u>87.0</u>	5.72	95.7	<u>7.36</u>	<u>93.9</u>	<u>2.31</u>
DA V2	<u>4.20</u>	98.2	5.61	96.8	4.73	98.0	<u>3.48</u>	98.5	<u>1.25</u>	100	21.4	72.8	13.0	86.6	<u>5.33</u>	<u>96.1</u>	7.38	93.4	2.50
Ours	3.41	98.6	4.08	98.1	3.17	98.8	3.20	<u>98.1</u>	0.944	100	18.4	79.5	8.91	91.5	4.00	97.3	5.76	95.2	1.06

Table 3. Quantitative results for depth map estimation. Gray numbers denote models trained on respective benchmarks and thus excluded from ranking.

Method	NYUv2		ETH3D		iBims-1		Average		
	Mean _↓	Med. _↓	Rank _↓						
Perspective	5.38	4.39	13.6	11.9	10.6	9.30	9.86	8.53	5.00
WildCam	3.82	<u>3.20</u>	7.70	5.81	9.48	9.08	7.00	6.03	3.00
LeReS	19.4	19.6	8.26	7.19	18.4	17.5	15.4	14.8	5.53
DUST3R	2.57	1.86	<u>5.77</u>	<u>3.60</u>	<u>3.83</u>	<u>2.53</u>	4.06	2.66	1.67
UniDepth	7.56	4.31	10.7	9.96	11.9	5.96	10.1	6.74	4.50
Ours	<u>3.41</u>	<u>3.21</u>	2.50	1.54	2.81	1.89	2.91	2.21	1.50

Table 4. Evaluation results for camera FoV in degrees.

Ablation	Point						Depth			Disparity		
	Scale-inv.		Affine-inv.		Local		Scale-inv.		Affine-inv.		Affine-inv.	
	Rel ^P _↓	δ ₁ ^P _↑	Rel ^P _↓	δ ₁ ^P _↑	Rel ^P _↓	δ ₁ ^P _↑	Rel ^d _↓	δ ₁ ^d _↑	Rel ^d _↓	δ ₁ ^d _↑	Rel ^d _↓	δ ₁ ^d _↑
Depth+camera	11.3	88.7	9.20	90.4	10.1	91.2	8.97	90.1	7.29	92.6	8.22	92.1
Opt. scale-inv.	10.5	89.7	8.50	91.4	9.09	92.0	8.28	90.9	6.72	93.3	7.91	92.6
Opt. affine-inv.	10.1	90.3	8.07	91.9	7.84	93.2	7.92	91.2	6.29	93.7	7.43	93.2
Med. affine-inv.	11.5	88.5	9.36	89.7	10.2	90.9	9.11	89.7	7.38	92.4	8.53	92.0
Full w/o clip	10.1	90.4	8.13	91.4	6.94	94.0	7.94	91.4	6.31	93.5	7.45	93.1
Full w/o L_S	10.1	90.2	8.10	91.8	7.51	93.5	7.94	91.2	6.31	93.6	7.47	93.2
Full	10.0	90.5	8.00	91.8	<u>7.07</u>	94.0	7.84	91.4	6.21	93.8	7.31	93.3

Table 5. Quantitative ablation study results. All experiments are conducted with a ViT-Base backbone for the encoder.

UniDepth [41], and DUST3R [57]. LeReS and UniDepth predict depth and camera parameters from single images. DUST3R is designed for two-view input and directly outputs camera-space point maps. It accepts two identical images for handling monocular scenarios. We evaluate both scale-invariant point maps in camera space and affine-invariant

point maps. Table 2 demonstrates that our method outperforms existing methods across most benchmarks, achieving the lowest average Rel^P for both point maps representations.

To further evaluate local geometry accuracy, we assess affine-invariant point maps within local regions defined by object segmentation masks, either from the dataset labels or

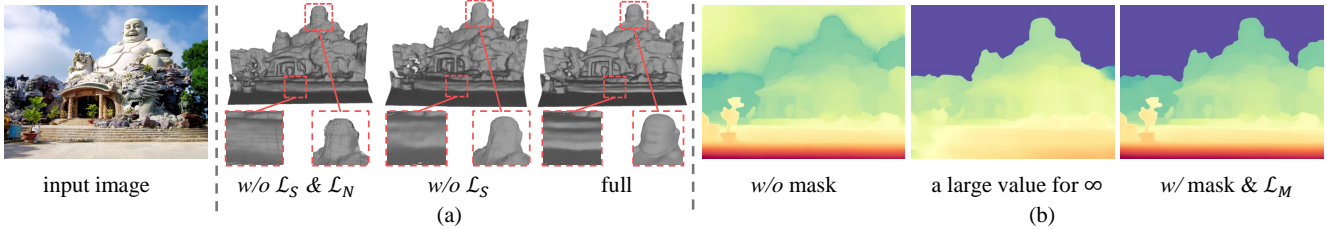


Figure 6. Qualitative ablation study results. All experiments use the ViT-Base backbone for the encoder. **(a)** Surface visualization of the impact of \mathcal{L}_S and \mathcal{L}_N . Removing either leads to noisy surfaces and poor geometry. **(b)** Depth visualization for the ablation of valid region mask prediction. Our method correctly predicts the sky regions, for which the predicted point values will be erroneous if the masks are removed. Supervising infinity regions by assigning a large distance label can negatively affect the foreground prediction accuracy.

obtained using Segment Anything [30]. Since per-region point map evaluation demands high-quality ground truth labels as well as the composition of multiple objects in a scene, NYUv2, KITTI, and GSO are excluded. Compared to the previous methods, our method significantly reduces the region-wise Rel^p by a large margin: from 7.96 to 5.33, achieving approximately a 30% error reduction.

Depth map estimation. We employ the same benchmarks used for point map evaluation to assess the depth estimation accuracy. We adopt absolute relative error Rel^d , *i.e.*, $|z - \hat{z}|/z$, and percentage of inliers δ_1^d with $\max(z/\hat{z}, \hat{z}/z) < 1.25$ as the evaluation metrics.

To conduct a comprehensive comparison with different monocular depth estimation methods, we evaluate scale-invariant depth [5, 26, 41, 57, 69], affine-invariant depth [20, 29], and affine-invariant disparity [6, 65, 66]. The z coordinates in our predicted point maps represent affine-invariant depth. By utilizing the camera shifts derived from Eq. 2, we convert these coordinates into scale-invariant depth. For affine-invariant disparity, we take the inverse of our scale-invariant depth predictions.

As shown in Table 3, our method achieves the best performance across most benchmarks and exhibits the lowest average Rel^d for all depth representations. Since existing methods with scale-invariant depth representations can be converted to affine-invariant depth and disparity, we provide an extensive comparison in the *suppl. materials*, where our method also significantly outperforms the others.

Camera FoV estimation. To evaluate the accuracy of the estimated camera FoV, we select benchmarks with vertical FoV $\geq 45^\circ$, including NYUv2 [38], ETH3D [49] and iBims-1 [31], and augment the FoV by randomly center cropping 50%~100% from the original images. All input images are undistorted and have a centered principal point.

We compare our model to point map estimation methods [41, 57, 69] as well as two learning-based camera calibration methods: Perspective [28] and WildCam [75]. For fair assessments of zero-shot performance, we utilize their pre-trained checkpoints on in-the-wild datasets. Mean and median FoV errors are reported in Table 4. Our method

achieves a mean error of 2.91° and a median error of 2.21° on average of the three FoV benchmarks, outperforming both camera calibration methods and point map estimation methods.

4.2. Qualitative comparison

We show visual results of disparity and point maps of different methods in Fig. 7. For depth prediction methods that do not recover camera parameters, we lift their results to 3D points using ground-truth intrinsics when available. Upon visual inspection, our method produces significantly less-distorted point maps compared to others, demonstrating its superior generalizability and accuracy. For example, as shown in the fourth row of Fig. 7, other methods result in noticeable stretching and deformation of the car shape. Although [66] produces visually sharp disparity maps, distorted 3D geometry can be observed even when provided with ground-truth camera intrinsics. In contrast, our method yields a more regular and well-formed car structure.

4.3. Ablation Study

We conducted comprehensive ablation studies on our point map representation, alignment strategy and loss function designs. For efficiency, we use the ViT-base model as backbone for these experiments.

Point map representation. Our method predicts affine-invariant point maps. Here we compare this representation with two variants, one scale-invariant point map in camera space, and another that predicts a depth maps and camera parameters. For the former, we apply the proposed ROE alignment solver to solve the scale parameter only. For the latter, we adopt the SI-log loss [18] for the depth map and the MSE loss for the ray direction map, similar to UniDepth [41]. The first three rows of Table 5 show the results of different approaches. In these experiments, only the global ground-truth supervision is applied during training. Our proposed affine-invariant representation outperforms the other variants across various tasks. This can be attributed to the fact that the other two variants suffer

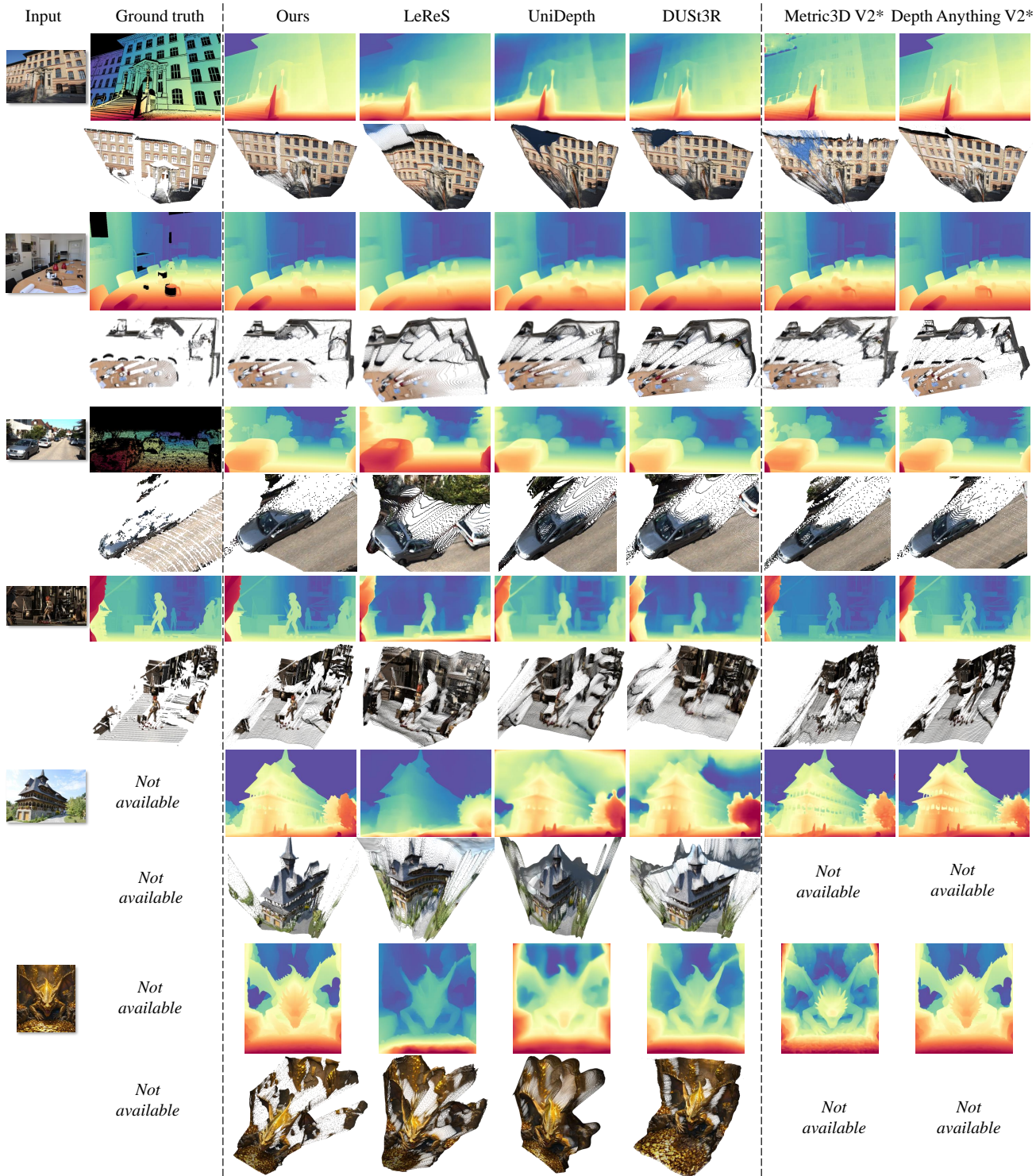


Figure 7. Qualitative comparison of point and disparity maps. *: for methods without camera intrinsics prediction, we use ground-truth camera intrinsics or disparity shifts to lift their results into 3D points when available. The first four cases are samples from our test datasets, while the last two are random “in-the-wild” images.

from focal-distance ambiguity issue during training which jeopardizes their performance.

Optimal alignment. To evaluate the effectiveness of our optimal alignment, we compare it to a previously-used simple alignment method [42], *i.e.*, we normalize the predicted and ground-truth point maps by their median z : $(\mathbf{p} - \mathbf{t}(\mathbf{P}))/s(\mathbf{P})$, where $\mathbf{t}(\mathbf{P})$ equals to $(0, 0, \text{median}(\mathbf{Z}))$, and $s(\mathbf{P})$ is computed as $\frac{1}{N} \sum_{i=1}^N \|\mathbf{p}_i - \mathbf{t}(\mathbf{P})\|_1$. As shown in the third and fourth rows of Table 5, our proposed alignment method consistently outperforms the median alignment strategy across all tasks by large margins, demonstrating the critical role of our proposed optimal alignment.

Multi-scale local geometry loss. As shown in the six-th row of Table 5, the quantitative results without \mathcal{L}_S suffer a significant drop on local geometry metrics. This demonstrates the effectiveness of \mathcal{L}_S in enhancing local geometry accuracy and compensating for the insufficient supervision of the global loss due to the ambiguous relative positions between distant scene objects. Fig. 6 (a) further demonstrates the effectiveness of the proposed local geometry loss.

Infinity mask. Our method predicts a valid region mask to handle regions at infinity. As shown in Fig. 6 (b), our method correctly predicts the sky regions, for which the predicted point values will be erroneous if the masks are removed. We further compare our mask prediction design with another strategy for addressing infinity. Specifically, we assign a large value, *i.e.*, 1,000 times the average distance of valid regions, to the infinity regions. Fig. 6 (b) shows that this strategy compromises the accuracy of foreground predictions as the network struggles to generate large values for infinity. Incorporating a separate mask prediction offers a convenient solution for masking out infinity and retaining accurate foreground geometry learning.

5. Conclusion

We have presented a method for accurate monocular geometry estimation of open-domain images. Our key insight is to design effective supervision which is largely neglected by previous methods. We propose a new affine-invariant point map representation which precludes ambiguous supervision during training. A robust, optimal, and efficient point map alignment solver is introduced for accurate global shape learning, together with a multi-scale local geometry loss designed for precise local geometry supervision. Trained on a large dataset collection, our model demonstrates strong generalizability and high accuracy for open-domain images. It significantly outperforms previous methods across various tasks and benchmarks. We believe our method marks a significant advancement in monocular 3D geometry estimation and can serve as a robust foundation model for various vision applications.

References

- [1] Sameer Agarwal, Yasutaka Furukawa, Noah Snavely, Ian Simon, Brian Curless, Steven M Seitz, and Richard Szeliski. Building rome in a day. *Communications of the ACM*, 54(10):105–112, 2011. 2
- [2] Eirikur Agustsson and Radu Timofte. Ntire 2017 challenge on single image super-resolution: Dataset and study. In *The IEEE Conference on Computer Vision and Pattern Recognition (CVPR) Workshops*, 2017. 4
- [3] Gilad Baruch, Zhuoyuan Chen, Afshin Dehghan, Tal Dimry, Yuri Feigin, Peter Fu, Thomas Gebauer, Brandon Joffe, Daniel Kurz, Arik Schwartz, and Elad Shulman. ARK-itscenes - a diverse real-world dataset for 3d indoor scene understanding using mobile RGB-d data. In *Thirty-fifth Conference on Neural Information Processing Systems Datasets and Benchmarks Track (Round 1)*, 2021. 3
- [4] Shariq Farooq Bhat, Ibraheem Alhashim, and Peter Wonka. Adabins: Depth estimation using adaptive bins. In *Proceedings of the IEEE/CVF conference on computer vision and pattern recognition*, pages 4009–4018, 2021. 3
- [5] Shariq Farooq Bhat, Reiner Birkel, Diana Wofk, Peter Wonka, and Matthias Müller. Zoedepth: Zero-shot transfer by combining relative and metric depth. *arXiv preprint arXiv:2302.12288*, 2023. 3, 6, 8
- [6] Reiner Birkel, Diana Wofk, and Matthias Müller. Midas v3. 1—a model zoo for robust monocular relative depth estimation. *arXiv preprint arXiv:2307.14460*, 2023. 6, 8
- [7] Oleksandr Bogdan, Viktor Eckstein, Francois Rameau, and Jean-Charles Bazin. Deepcalib: A deep learning approach for automatic intrinsic calibration of wide field-of-view cameras. In *Proceedings of the 15th ACM SIGGRAPH European Conference on Visual Media Production*, pages 1–10, 2018. 3
- [8] Stephen Boyd and Lieven Vandenberghe. *Convex Optimization*. Cambridge University Press, New York, NY, USA, 2004. 5
- [9] D. J. Butler, J. Wulff, G. B. Stanley, and M. J. Black. A naturalistic open source movie for optical flow evaluation. In *European Conf. on Computer Vision (ECCV)*, pages 611–625. Springer-Verlag, 2012. 6, 3
- [10] Weifeng Chen, Zhao Fu, Dawei Yang, and Jia Deng. Single-image depth perception in the wild. In *Advances in Neural Information Processing Systems*. Curran Associates, Inc., 2016. 3
- [11] Weifeng Chen, Shengyi Qian, David Fan, Noriyuki Kojima, Max Hamilton, and Jia Deng. Oasis: A large-scale dataset for single image 3d in the wild. In *Proceedings of the IEEE/CVF Conference on Computer Vision and Pattern Recognition (CVPR)*, 2020. 3
- [12] Matt Deitke, Dustin Schwenk, Jordi Salvador, Luca Weihs, Oscar Michel, Eli VanderBilt, Ludwig Schmidt, Kiana Ehsani, Aniruddha Kembhavi, and Ali Farhadi. Objaverse: A universe of annotated 3d objects. In *Proceedings of the IEEE/CVF Conference on Computer Vision and Pattern Recognition*, pages 13142–13153, 2023. 3
- [13] Jonathan Deutscher, Michael Isard, and John MacCormick. Automatic camera calibration from a single manhattan im-

- age. In *Computer Vision—ECCV 2002: 7th European Conference on Computer Vision Copenhagen, Denmark, May 28–31, 2002 Proceedings, Part IV* 7, pages 175–188. Springer, 2002. 3
- [14] Digital Image Media Laboratory (DIML) and Computer Vision Laboratory (CVL). Diml/cvl rgb-d dataset: 2m rgb-d images of natural indoor and outdoor scenes. https://dimlrgbd.github.io/downloads/technical_report.pdf. 3
- [15] Alexey Dosovitskiy, Lucas Beyer, Alexander Kolesnikov, Dirk Weissenborn, Xiaohua Zhai, Thomas Unterthiner, Mostafa Dehghani, Matthias Minderer, Georg Heigold, Sylvain Gelly, Jakob Uszkoreit, and Neil Houlsby. An image is worth 16x16 words: Transformers for image recognition at scale. *ICLR*, 2021. 3, 6
- [16] Laura Downs, Anthony Francis, Nate Koenig, Brandon Kinman, Ryan Hickman, Krista Reymann, Thomas B. McHugh, and Vincent Vanhoucke. Google scanned objects: A high-quality dataset of 3d scanned household items, 2022. 6, 3
- [17] Ainaz Eftekhari, Alexander Sax, Jitendra Malik, and Amir Zamir. Omnidata: A scalable pipeline for making multi-task mid-level vision datasets from 3d scans. In *Proceedings of the IEEE/CVF International Conference on Computer Vision*, pages 10786–10796, 2021. 3
- [18] David Eigen, Christian Puhrsch, and Rob Fergus. Depth map prediction from a single image using a multi-scale deep network. *Advances in neural information processing systems*, 27, 2014. 3, 8
- [19] Michael Fonder and Marc Van Droogenbroeck. Mid-air: A multi-modal dataset for extremely low altitude drone flights. In *Conference on Computer Vision and Pattern Recognition Workshop (CVPRW)*, 2019. 3
- [20] Xiao Fu, Wei Yin, Mu Hu, Kaixuan Wang, Yuexin Ma, Ping Tan, Shaojie Shen, Dahua Lin, and Xiaoxiao Long. Geowizard: Unleashing the diffusion priors for 3d geometry estimation from a single image. *arXiv preprint arXiv:2403.12013*, 2024. 2, 3, 5, 6, 8
- [21] Jakob Geyer, Yohannes Kassahun, Mentar Mahmudi, Xavier Ricou, Rupesh Durgesh, Andrew S. Chung, Lorenz Hauswald, Viet Hoang Pham, Maximilian Mühlegg, Sebastian Dorn, Tiffany Fernandez, Martin Jänicke, Sudesh Mirashi, Chiragkumar Savani, Martin Sturm, Oleksandr Vorobiov, Martin Oelker, Sebastian Garreis, and Peter Schuberth. A2D2: Audi Autonomous Driving Dataset. 2020. 3
- [22] Clément Godard, Oisín Mac Aodha, Michael Firman, and Gabriel J Brostow. Digging into self-supervised monocular depth estimation. In *Proceedings of the IEEE/CVF international conference on computer vision*, pages 3828–3838, 2019. 3
- [23] Ming Gui, Johannes S Fischer, Ulrich Prestel, Pingchuan Ma, Dmytro Kotovenko, Olga Grebenkova, Stefan Andreas Baumann, Vincent Tao Hu, and Björn Ommer. Depthfm: Fast monocular depth estimation with flow matching. *arXiv preprint arXiv:2403.13788*, 2024. 3
- [24] Vitor Guizilini, Rares Ambrus, Sudeep Pillai, Allan Ravenstos, and Adrien Gaidon. 3d packing for self-supervised monocular depth estimation. In *IEEE Conference on Computer Vision and Pattern Recognition (CVPR)*, 2020. 6, 3
- [25] Jose L. Gómez, Manuel Silva, Antonio Seoane, Agnès Borrás, Mario Noriega, Germán Ros, Jose A. Iglesias-Guitián, and Antonio M. López. All for one, and one for all: Urbansyn dataset, the third musketeer of synthetic driving scenes, 2023. 3
- [26] Mu Hu, Wei Yin, Chi Zhang, Zhipeng Cai, Xiaoxiao Long, Hao Chen, Kaixuan Wang, Gang Yu, Chunhua Shen, and Shaojie Shen. Metric3d v2: A versatile monocular geometric foundation model for zero-shot metric depth and surface normal estimation. *arXiv preprint arXiv:2404.15506*, 2024. 3, 6, 8, 4
- [27] Po-Han Huang, Kevin Matzen, Johannes Kopf, Narendra Ahuja, and Jia-Bin Huang. Deepmvs: Learning multi-view stereopsis. In *IEEE Conference on Computer Vision and Pattern Recognition (CVPR)*, 2018. 3
- [28] Linyi Jin, Jianming Zhang, Yannick Hold-Geoffroy, Oliver Wang, Kevin Blackburn-Matzen, Matthew Sticha, and David F Fouhey. Perspective fields for single image camera calibration. In *Proceedings of the IEEE/CVF Conference on Computer Vision and Pattern Recognition*, pages 17307–17316, 2023. 3, 6, 8
- [29] Bingxin Ke, Anton Obukhov, Shengyu Huang, Nando Metzger, Rodrigo Caye Daudt, and Konrad Schindler. Repurposing diffusion-based image generators for monocular depth estimation. In *Proceedings of the IEEE/CVF Conference on Computer Vision and Pattern Recognition*, pages 9492–9502, 2024. 2, 3, 5, 6, 8
- [30] Alexander Kirillov, Eric Mintun, Nikhila Ravi, Hanzi Mao, Chloe Rolland, Laura Gustafson, Tete Xiao, Spencer Whitehead, Alexander C Berg, Wan-Yen Lo, et al. Segment anything. In *Proceedings of the IEEE/CVF International Conference on Computer Vision*, pages 4015–4026, 2023. 8
- [31] Tobias Koch, Lukas Liebel, Marco Körner, and Friedrich Fraundorfer. Comparison of monocular depth estimation methods using geometrically relevant metrics on the ibims-1 dataset. *Computer Vision and Image Understanding (CVIU)*, 191:102877, 2020. 6, 8, 3
- [32] Jinwoo Lee, Hyunsung Go, Hyunjoon Lee, Sunghyun Cho, Minhyuk Sung, and Junho Kim. Ctrl-c: Camera calibration transformer with line-classification. In *Proceedings of the IEEE/CVF International Conference on Computer Vision*, pages 16228–16237, 2021. 3
- [33] Yixuan Li, Lihan Jiang, Linning Xu, Yuanbo Xiangli, Zhenzhi Wang, Dahua Lin, and Bo Dai. Matrixcity: A large-scale city dataset for city-scale neural rendering and beyond. In *Proceedings of the IEEE/CVF International Conference on Computer Vision*, pages 3205–3215, 2023. 3
- [34] Zhengqi Li and Noah Snavely. Megadepth: Learning single-view depth prediction from internet photos. In *Computer Vision and Pattern Recognition (CVPR)*, 2018. 3
- [35] Zhenyu Li, Xuyang Wang, Xianming Liu, and Junjun Jiang. Binsformer: Revisiting adaptive bins for monocular depth estimation. *IEEE Transactions on Image Processing*, 2024. 3
- [36] Lukas Mehl, Jenny Schmalzfuss, Azin Jahedi, Yaroslava Nalivayko, and Andrés Bruhn. Spring: A high-resolution high-detail dataset and benchmark for scene flow, optical flow and

- stereo. In *Proc. IEEE/CVF Conference on Computer Vision and Pattern Recognition (CVPR)*, 2023. 3
- [37] Jorge J Moré. The levenberg-marquardt algorithm: implementation and theory. In *Numerical analysis: proceedings of the biennial Conference held at Dundee, June 28–July 1, 1977*, pages 105–116. Springer, 2006. 1
- [38] Pushmeet Kohli Nathan Silberman, Derek Hoiem and Rob Fergus. Indoor segmentation and support inference from rgbd images. In *ECCV*, 2012. 6, 8, 3
- [39] Simon Niklaus, Long Mai, Jimei Yang, and Feng Liu. 3d ken burns effect from a single image. *ACM Transactions on Graphics*, 38(6):184:1–184:15, 2019. 3
- [40] Maxime Oquab, Timothée Darcet, Théo Moutakanni, Huy Vo, Marc Szafraniec, Vasil Khalidov, Pierre Fernandez, Daniel Haziza, Francisco Massa, Alaaeldin El-Nouby, et al. Dinov2: Learning robust visual features without supervision. *arXiv preprint arXiv:2304.07193*, 2023. 3, 6
- [41] Luigi Piccinelli, Yung-Hsu Yang, Christos Sakaridis, Mattia Segu, Siyuan Li, Luc Van Gool, and Fisher Yu. Unidepth: Universal monocular metric depth estimation. In *Proceedings of the IEEE/CVF Conference on Computer Vision and Pattern Recognition*, pages 10106–10116, 2024. 2, 3, 6, 7, 8, 4
- [42] René Ranftl, Katrin Lasinger, David Hafner, Konrad Schindler, and Vladlen Koltun. Towards robust monocular depth estimation: Mixing datasets for zero-shot cross-dataset transfer. *IEEE transactions on pattern analysis and machine intelligence*, 44(3):1623–1637, 2020. 3, 5, 10
- [43] René Ranftl, Alexey Bochkovskiy, and Vladlen Koltun. Vision transformers for dense prediction. In *Proceedings of the IEEE/CVF international conference on computer vision*, pages 12179–12188, 2021. 3
- [44] Mike Roberts, Jason Ramapuram, Anurag Ranjan, Atulit Kumar, Miguel Angel Bautista, Nathan Paczan, Russ Webb, and Joshua M. Susskind. Hypersim: A photorealistic synthetic dataset for holistic indoor scene understanding. In *International Conference on Computer Vision (ICCV) 2021*, 2021. 3
- [45] Robin Rombach, Andreas Blattmann, Dominik Lorenz, Patrick Esser, and Björn Ommer. High-resolution image synthesis with latent diffusion models, 2021. 6
- [46] German Ros, Laura Sellart, Joanna Materzynska, David Vazquez, and Antonio M. Lopez. The synthia dataset: A large collection of synthetic images for semantic segmentation of urban scenes. In *The IEEE Conference on Computer Vision and Pattern Recognition (CVPR)*, 2016. 3
- [47] Johannes L Schonberger and Jan-Michael Frahm. Structure-from-motion revisited. In *Proceedings of the IEEE conference on computer vision and pattern recognition*, pages 4104–4113, 2016. 2
- [48] Johannes L Schönberger, Enliang Zheng, Jan-Michael Frahm, and Marc Pollefeys. Pixelwise view selection for unstructured multi-view stereo. In *Computer Vision–ECCV 2016: 14th European Conference, Amsterdam, The Netherlands, October 11–14, 2016, Proceedings, Part III 14*, pages 501–518. Springer, 2016. 2
- [49] Thomas Schöps, Torsten Sattler, and Marc Pollefeys. BAD SLAM: Bundle adjusted direct RGB-D SLAM. In *Conference on Computer Vision and Pattern Recognition (CVPR)*, 2019. 6, 8, 3
- [50] Pei Sun, Henrik Kretschmar, Xerxes Dotiwalla, Aurelien Chouard, Vijaysai Patnaik, Paul Tsui, James Guo, Yin Zhou, Yuning Chai, Benjamin Caine, Vijay Vasudevan, Wei Han, Jiquan Ngiam, Hang Zhao, Aleksei Timofeev, Scott Etinger, Maxim Krivokon, Amy Gao, Aditya Joshi, Yu Zhang, Jonathon Shlens, Zhifeng Chen, and Dragomir Anguelov. Scalability in perception for autonomous driving: Waymo open dataset. In *Proceedings of the IEEE/CVF Conference on Computer Vision and Pattern Recognition (CVPR)*, 2020. 3
- [51] Jonas Uhrig, Nick Schneider, Lukas Schneider, Uwe Franke, Thomas Brox, and Andreas Geiger. Sparsity invariant cnns. In *International Conference on 3D Vision (3DV)*, 2017. 6, 3
- [52] Igor Vasiljevic, Nick Kolkin, Shanyi Zhang, Ruotian Luo, Haochen Wang, Falcon Z. Dai, Andrea F. Daniele, Mohammadreza Mostajabi, Steven Basart, Matthew R. Walter, and Gregory Shakhnarovich. DIODE: A Dense Indoor and Outdoor DDepth Dataset. *CoRR*, abs/1908.00463, 2019. 6, 3
- [53] Pauli Virtanen, Ralf Gommers, Travis E. Oliphant, Matt Haberland, Tyler Reddy, David Cournapeau, Evgeni Burovski, Pearu Peterson, Warren Weckesser, Jonathan Bright, Stéfan J. van der Walt, Matthew Brett, Joshua Wilson, K. Jarrod Millman, Nikolay Mayorov, Andrew R. J. Nelson, Eric Jones, Robert Kern, Eric Larson, C J Carey, İlhan Polat, Yu Feng, Eric W. Moore, Jake VanderPlas, Denis Laxalde, Josef Perktold, Robert Cimrman, Ian Henriksen, E. A. Quintero, Charles R. Harris, Anne M. Archibald, Antônio H. Ribeiro, Fabian Pedregosa, Paul van Mulbregt, and SciPy 1.0 Contributors. SciPy 1.0: Fundamental Algorithms for Scientific Computing in Python. *Nature Methods*, 17:261–272, 2020. 1
- [54] Qiang Wan, Zilong Huang, Bingyi Kang, Jiashi Feng, and Li Zhang. Harnessing diffusion models for visual perception with meta prompts. *arXiv preprint arXiv:2312.14733*, 2023. 3
- [55] Kaixuan Wang and Shaojie Shen. Flow-motion and depth network for monocular stereo and beyond. *CoRR*, abs/1909.05452, 2019. 3
- [56] Qiang Wang, Shizhen Zheng, Qingsong Yan, Fei Deng, Kaiyong Zhao, and Xiaowen Chu. IRS: A large synthetic indoor robotics stereo dataset for disparity and surface normal estimation. *CoRR*, abs/1912.09678, 2019. 3
- [57] Shuzhe Wang, Vincent Leroy, Yohann Cabon, Boris Chidlovskii, and Jerome Revaud. Dust3r: Geometric 3d vision made easy. In *CVPR*, 2024. 2, 3, 4, 6, 7, 8
- [58] Wenshan Wang, DeLong Zhu, Xiangwei Wang, Yaoyu Hu, Yuheng Qiu, Chen Wang, Yafei Hu, Ashish Kapoor, and Sebastian Scherer. Tartanair: A dataset to push the limits of visual slam. 2020. 3
- [59] Marta Wilczkowiak, Edmond Boyer, and Peter Sturm. Camera calibration and 3d reconstruction from single images using parallelepipeds. In *IEEE International Conference on Computer Vision*, pages 142–148. IEEE, 2001. 3

- [60] Benjamin Wilson, William Qi, Tanmay Agarwal, John Lambert, Jagjeet Singh, Siddhesh Khandelwal, Bowen Pan, Ratnesh Kumar, Andrew Hartnett, Jhony Kaesemodel Pontes, Deva Ramanan, Peter Carr, and James Hays. Argoverse 2: Next generation datasets for self-driving perception and forecasting. In *Proceedings of the Neural Information Processing Systems Track on Datasets and Benchmarks (NeurIPS Datasets and Benchmarks 2021)*, 2021. 3
- [61] Scott Workman, Connor Greenwell, Menghua Zhai, Ryan Baltenberger, and Nathan Jacobs. Deepfocal: A method for direct focal length estimation. In *2015 IEEE International Conference on Image Processing (ICIP)*, pages 1369–1373. IEEE, 2015. 3
- [62] Enze Xie, Wenhai Wang, Zhiding Yu, Anima Anandkumar, Jose M Alvarez, and Ping Luo. Segformer: Simple and efficient design for semantic segmentation with transformers. *Advances in neural information processing systems*, 34: 12077–12090, 2021. 6
- [63] Saining Xie, Ross Girshick, Piotr Dollár, Zhuowen Tu, and Kaiming He. Aggregated residual transformations for deep neural networks. In *Proceedings of the IEEE conference on computer vision and pattern recognition*, pages 1492–1500, 2017. 6
- [64] Jiayu Yang, Wei Mao, Jose M Alvarez, and Miaomiao Liu. Cost volume pyramid based depth inference for multi-view stereo. In *Proceedings of the IEEE/CVF conference on computer vision and pattern recognition*, pages 4877–4886, 2020. 2
- [65] Lihe Yang, Bingyi Kang, Zilong Huang, Xiaogang Xu, Jiashi Feng, and Hengshuang Zhao. Depth anything: Unleashing the power of large-scale unlabeled data. In *Proceedings of the IEEE/CVF Conference on Computer Vision and Pattern Recognition*, pages 10371–10381, 2024. 2, 3, 5, 6, 8
- [66] Lihe Yang, Bingyi Kang, Zilong Huang, Zhen Zhao, Xiaogang Xu, Jiashi Feng, and Hengshuang Zhao. Depth anything v2. *arXiv preprint arXiv:2406.09414*, 2024. 3, 5, 6, 8, 4
- [67] Yao Yao, Zixin Luo, Shiwei Li, Jingyang Zhang, Yufan Ren, Lei Zhou, Tian Fang, and Long Quan. Blendedmvs: A large-scale dataset for generalized multi-view stereo networks. *Computer Vision and Pattern Recognition (CVPR)*, 2020. 3
- [68] Wei Yin, Xinlong Wang, Chunhua Shen, Yifan Liu, Zhi Tian, Songcen Xu, Changming Sun, and Dou Renyin. Diversedepth: Affine-invariant depth prediction using diverse data. *arXiv preprint arXiv:2002.00569*, 2020. 3
- [69] Wei Yin, Jianming Zhang, Oliver Wang, Simon Niklaus, Long Mai, Simon Chen, and Chunhua Shen. Learning to recover 3d scene shape from a single image. *CoRR*, abs/2012.09365, 2020. 2, 3, 6, 8, 4
- [70] Wei Yin, Jianming Zhang, Oliver Wang, Simon Niklaus, Simon Chen, Yifan Liu, and Chunhua Shen. Towards accurate reconstruction of 3d scene shape from a single monocular image. *IEEE Transactions on Pattern Analysis and Machine Intelligence*, 45(5):6480–6494, 2022. 3
- [71] Wei Yin, Chi Zhang, Hao Chen, Zhipeng Cai, Gang Yu, Kaixuan Wang, Xiaozhi Chen, and Chunhua Shen. Metric3d: Towards zero-shot metric 3d prediction from a single image. In *Proceedings of the IEEE/CVF International Conference on Computer Vision*, pages 9043–9053, 2023. 2, 3
- [72] Amir R Zamir, Alexander Sax, , William B Shen, Leonidas Guibas, Jitendra Malik, and Silvio Savarese. Taskonomy: Disentangling task transfer learning. In *2018 IEEE Conference on Computer Vision and Pattern Recognition (CVPR)*. IEEE, 2018. 3
- [73] Zhengyou Zhang. A flexible new technique for camera calibration. *IEEE Transactions on Pattern Analysis and Machine Intelligence*, 22(11):1330–1334, 2000. 3
- [74] Jia Zheng, Junfei Zhang, Jing Li, Rui Tang, Shenghua Gao, and Zihan Zhou. Structured3d: A large photo-realistic dataset for structured 3d modeling. In *Proceedings of The European Conference on Computer Vision (ECCV)*, 2020. 3
- [75] Shengjie Zhu, Abhinav Kumar, Masa Hu, and Xiaoming Liu. Tame a wild camera: in-the-wild monocular camera calibration. *Advances in Neural Information Processing Systems*, 36, 2024. 3, 6, 8

MoGe: Unlocking Accurate Monocular Geometry Estimation for Open-Domain Images with Optimal Training Supervision

Supplementary Material

A. Algorithm details

A.1. Recovering shift and camera focal

We assume a simple pinhole camera model with isotropic focal length and centered principal point. The 2D image plane is parameterized with the center as $(0, 0)$. The image plane coordinate of pixel i is denoted as (u_i, v_i) , corresponding to its predicted 3D point $\mathbf{p}_i = (x_i, y_i, z_i)$. The focal length and shift is obtained by minimizing the projection error,

$$\min_{f, t_z} \sum_{i \in \mathcal{M}} \left(\frac{fx_i}{z_i + t_z} - u_i \right)^2 + \left(\frac{fy_i}{z_i + t_z} - v_i \right)^2 \quad (9)$$

which can be further reduced to have a single variable t'_z by substituting f with its close-form solution with respect to t'_z

$$f = \frac{\sum_{i \in \mathcal{M}} \left(\frac{x_i}{z_i + t'_z} \right) u_i + \sum_{i \in \mathcal{M}} \left(\frac{y_i}{z_i + t'_z} \right) v_i}{\sum_{i \in \mathcal{M}} \left(\frac{x_i}{z_i + t'_z} \right)^2 + \sum_{i \in \mathcal{M}} \left(\frac{y_i}{z_i + t'_z} \right)^2} \quad (10)$$

We use a numerical solver for this least squares problem with Levenberg-Marquardt algorithm [37] implemented by SciPy [53] package. For efficiency, the point map is resized to low resolution (64×64) for running this algorithm. In our practice, it typically converges within 10 iterations in around 3ms.

A.2. Optimal alignment

We will first introduce an algorithm to a simpler subproblem then derive the solution to either with or without the constraint of $t_x = t_y = 0$ (1D-shift case or 3D-shift case, respectively).

Subproblem (w/o clipping) Consider the optimization objective with respect to scale s only, denoted as $l_0(s)$. We omit the mask \mathcal{M} for simplicity and denote N as the number of valid points.

$$\min_s l_0(s) = \min_s \sum_{i=1}^N w_i |s\hat{x}_i - x_i| \quad (11)$$

where $w_i > 0$ and $\hat{x}_i > 0$ without loss of generality. The objective, as a summation of convex functions, is also convex obviously. The minimum occurs where its left-hand

$l_0^-(s)$ derivative and right-hand derivative $l_0^+(s)$ have opposite signs or one of them is zero,

$$\begin{aligned} l_0^-(s) &= \sum_{\frac{x_i}{\hat{x}_i} < s} w_i \hat{x}_i - \sum_{s \leq \frac{x_i}{\hat{x}_i}} w_i \hat{x}_i \\ &= 2 \sum_{\frac{x_i}{\hat{x}_i} < s} w_i \hat{x}_i - \sum_{i=1}^N w_i \hat{x}_i \\ l_0^+(s) &= \sum_{\frac{x_i}{\hat{x}_i} \leq s} w_i \hat{x}_i - \sum_{s < \frac{x_i}{\hat{x}_i}} w_i \hat{x}_i \\ &= 2 \sum_{\frac{x_i}{\hat{x}_i} \leq s} w_i \hat{x}_i - \sum_{i=1}^N w_i \hat{x}_i \end{aligned} \quad (12)$$

$l_0^-(s)$ and $l_0^+(s)$ differ at $\left\{ \frac{x_i}{\hat{x}_i} \right\}$. One might first sort $\left\{ \frac{x_i}{\hat{x}_i} \right\}$ and compute the prefix summations of $\{w_i \hat{x}_i\}$. Then the derivatives can be evaluated in $O(1)$ time for each point in $\left\{ \frac{x_i}{\hat{x}_i} \right\}$. Finally, $\frac{\hat{x}_i}{x_i}$ such that $l_0^-\left(\frac{x_i}{\hat{x}_i}\right) < 0 \leq l_0^+\left(\frac{x_i}{\hat{x}_i}\right)$ is a deterministic minimum point.

Subproblem (w/ clipping) We clip each residual term to suppress the contribution of outliers. Specifically, the clipped objective is

$$\min_s l_1(s) = \min_s \sum_{i=1}^N \min(\tau, w_i |s\hat{x}_i - x_i|) \quad (13)$$

For each item $l_{1,i}(s) = \min(\tau, w_i |s\hat{x}_i - x_i|)$ in the equation, the one-sided derivatives are

$$\begin{aligned} l_{1,i}^-(s) &= \begin{cases} -w_i \hat{x}_i & \frac{w_i x_i - \tau_i}{w_i \hat{x}_i} < s \leq \frac{x_i}{\hat{x}_i} \\ w_i \hat{x}_i & \frac{x_i}{\hat{x}_i} < s \leq \frac{w_i x_i + \tau_i}{w_i \hat{x}_i} \\ 0 & \text{otherwise} \end{cases} \\ l_{1,i}^+(s) &= \begin{cases} -w_i \hat{x}_i & \frac{w_i x_i - \tau_i}{w_i \hat{x}_i} \leq s < \frac{x_i}{\hat{x}_i} \\ w_i \hat{x}_i & \frac{x_i}{\hat{x}_i} \leq s < \frac{w_i x_i + \tau_i}{w_i \hat{x}_i} \\ 0 & \text{otherwise} \end{cases} \end{aligned} \quad (14)$$

Therefore, the one-sided derivatives of $l_0(s)$ are

$$\begin{aligned}
l_1^-(s) &= \sum_{i=1}^N l_{1,i}^-(s) \\
&= \sum_{\frac{x_i}{\hat{x}_i} < s \leq \frac{w_i x_i + \tau}{w_i \hat{x}_i}} w_i \hat{x}_i - \sum_{\frac{w_i x_i - \tau}{w_i \hat{x}_i} < s \leq \frac{x_i}{\hat{x}_i}} w_i \hat{x}_i \\
&= 2 \sum_{\frac{x_i}{\hat{x}_i} < s} w_i \hat{x}_i - \sum_{\frac{w_i x_i - \tau}{w_i \hat{x}_i} < s} w_i \hat{x}_i - \sum_{\frac{w_i x_i + \tau}{w_i \hat{x}_i} < s} w_i \hat{x}_i
\end{aligned} \tag{15}$$

$$\begin{aligned}
l_1^+(s) &= \sum_{i=1}^N l_{1,i}^+(s) \\
&= \sum_{\frac{x_i}{\hat{x}_i} \leq s < \frac{w_i x_i + \tau}{w_i \hat{x}_i}} w_i \hat{x}_i - \sum_{\frac{w_i x_i - \tau}{w_i \hat{x}_i} \leq s < \frac{x_i}{\hat{x}_i}} w_i \hat{x}_i \\
&= 2 \sum_{\frac{x_i}{\hat{x}_i} \leq s} w_i \hat{x}_i - \sum_{\frac{w_i x_i - \tau}{w_i \hat{x}_i} \leq s} w_i \hat{x}_i - \sum_{\frac{w_i x_i + \tau}{w_i \hat{x}_i} \leq s} w_i \hat{x}_i
\end{aligned} \tag{16}$$

One can evaluate $l_1^+(s)$ efficiently through first binary searching on the sorted arrays $\left\{\frac{x_i}{\hat{x}_i}\right\}$, $\left\{\frac{w_i x_i - \tau}{w_i \hat{x}_i}\right\}$ and $\left\{\frac{w_i x_i + \tau}{w_i \hat{x}_i}\right\}$ and then indexing the precomputed prefix summations of $\{w_i \hat{x}_i\}$ in the associated orders.

Lemma 1. *There exists at least one pair of (k^*, s^*) such that $s^* x_{k^*} - \hat{x}_{k^*} = 0$ and s^* minimizes Eq. 13*

Proof. The minimum of $l_1(s)$ must exist, because $l_1(s)$ is continuous, piece-wisely linear and bounded in $[0, N\tau]$.

We first prove that there must exist s^* such that $l_1(s^*) = \min l_1(s)$ and $l_1^+(s^*) > l_1^-(s^*)$. Otherwise, for all s^* such that $l_0(s^*) = \min l_1(s)$, there will be $l_1^+(s^*) = l_1^-(s^*) = 0$, hence the value of $l_1(s)$ in the linear interval where the minimum locates is constant. As a consequence, all neighboring intervals will be constant until the boundary where $\min l_1(s) = l_1(-\infty) = N\tau$, which contradicts the obvious fact that $\min l_1(s) \leq l_1(x_1/\hat{x}_1) < N\tau$.

Given $l_0^+(s^*) > l_0^-(s^*)$, there exists an index k^* such that $s^* = \hat{x}_{k^*}/x_{k^*}$, because

$$\begin{aligned}
0 &< l_1^+(s^*) - l_1^-(s^*) \\
&= 2 \sum_{\frac{\hat{x}_i}{x_i} = s^*} w_i x_i - \sum_{\frac{w_i \hat{x}_i - \tau}{w_i x_i} = s^*} w_i x_i - \sum_{\frac{w_i \hat{x}_i + \tau}{w_i x_i} = s^*} w_i x_i \\
&< 2 \sum_{\frac{\hat{x}_i}{x_i} = s^*} w_i x_i
\end{aligned} \tag{17}$$

□

Lemma 1 has proved that the minimum point of the objective function in Eq. 13 still occurs among $\left\{\frac{x_i}{\hat{x}_i}\right\}$, although the function is non-convex and may contain local

minima. Therefore, it takes two steps to solve the sub-problem. First, find all extrema among $\left\{\frac{x_i}{\hat{x}_i}\right\}$ such that $l_0^-\left(\frac{x_i}{\hat{x}_i}\right) < 0 \leq l_0^+\left(\frac{x_i}{\hat{x}_i}\right)$ by evaluating the derivative values, which takes $O(N \log N)$ time. Second, evaluate the objective values of those extrema and then find the minimum, which takes $O(N n_e)$ time. n_e is the number of extrema, approximating the number of outliers, which is expected to be a small constant in practice.

Alignment with 1D shift Recall the objective in Eq. 4. Let w_i be $1/z_i$. We apply clipping to each absolute term and rewrite it as follows

$$\begin{aligned}
\min_{s, t_z} \sum_{i=1}^n \min(\tau, w_i |s \hat{x}_i - x_i|) + \min(\tau, w_i |s \hat{y}_i - y_i|) \\
+ \min(\tau, w_i |s \hat{z}_i + t_z - z_i|)
\end{aligned} \tag{18}$$

Lemma 2. *There exists at least one triplet of (k^*, s^*, t_z^*) such that $s^* \hat{z}_{k^*} + t_z^* - z_{k^*} = 0$ and (s^*, t_z^*) minimizes the objective of Equation 18.*

Proof. Denote the objective as $l_2(s, t_z)$,

$$\begin{aligned}
l_2(s, t_z) &= \sum_{i=1}^n \min(\tau, w_i |s \hat{x}_i - x_i|) \\
&+ \sum_{i=1}^n \min(\tau, w_i |s \hat{y}_i - y_i|) \\
&+ \sum_{i=1}^n \min(\tau, w_i |t_z - (z_i - s \hat{z}_i)|)
\end{aligned} \tag{19}$$

Given arbitrary s , using Lemma 1, there exists at least one pair (t_z, k) such that $t_z - (z_k - s \hat{z}_k) = 0$ and t_z minimizes $\sum_{i=1}^n \min(\tau, w_i |s \hat{z}_i + t_z - z_i|)$, hence minimizes $l_2(s, t_z)$ as the rest parts are constant with regard to t_z . Therefore, a solution s^* is always associated with corresponding (t_z^*, k^*) such that $s^* \hat{z}_{k^*} + t_z^* - z_{k^*} = 0$. □

Lemma 2 allows us to reduce Eq. 18 to the subproblem with respect to some index k . For each possible index k , the objective is formed as

$$\begin{aligned}
\min_s \sum_{i=1}^n \min(\tau, w_i |s \hat{x}_i - s x_i|) + \min(\tau, w_i |s \hat{y}_i - y_i|) \\
+ \min(\tau, w_i |s(\hat{z}_i - \hat{z}_k) - (z_i - z_k)|)
\end{aligned} \tag{20}$$

which is solvable in $O(N \log N)$ complexity. We enumerate all possible indices for k and find the minimum. Therefore, the total time complexity is $O(N^2 \log N)$.

In our implementation, the point map is resized to low resolution (64×64) for alignment, with $N = 4096$ at most. The algorithm is further parallelized with tensor operations on GPUs.

Alignment with 3D shift Similarly to the proof of Lemma 2, there exists at least one group $(k_1^*, k_2^*, k_3^*, s^*, \mathbf{t}^*)$ such that $s^* \hat{x}_{k_1^*} + t_x^* - x_{k_1^*} = 0$, $s^* \hat{y}_{k_2^*} + t_y^* - y_{k_2^*} = 0$, $s^* \hat{z}_{k_3^*} + t_z^* - z_{k_3^*} = 0$, and (s^*, \mathbf{t}^*) minimizes the objective. However, the $O(N^4 \log N)$ time complexity of a brute-force search is prohibitive. Motivated by the strong locality of surface points within a 3D sphere, we introduce a reasonable assumption, $k_1 = k_2 = k_3$, to obtain an approximately optimal solution with $O(N^2 \log N)$ complexity. This assumption posits that the predicted and ground truth patches can be well aligned under the condition that one corresponding pair of points coincides. The effectiveness of the approximated solution has been empirically validated.

B. Data details

B.1. Training data

The datasets used in our training are listed in Table 6. The number of frames may slightly differ from that of the original data because some invalid frames are dropped.

Name	Domain	#Frames	Type	Weight
Training				
A2D2[21]	Outdoor/Driving	196K	C	0.8%
Argoverse2[60]	Outdoor/Driving	1.1M	C	7.4%
ARKitScenes[3]	Indoor	449K	B	8.6%
DIML-indoor[14]	Indoor	894K	D	4.8%
BlendedMVS[67]	In-the-wild	115K	B	12.0%
MegaDepth[34]	Outdoor/In-the-wild	92K	B	5.6%
Taskonomy[72]	Indoor	3.6M	B	14.1%
Waymo[50]	Outdoor/Driving	788K	C	6.4%
GTA-SfM[55]	Outdoor/In-the-wild	19K	A	2.8%
Hypersim[44]	Indoor	75K	A	5.0%
IRS[56]	Indoor	101K	A	5.6%
KenBurns[39]	In-the-wild	76K	A	1.6%
MatrixCity[33]	Outdoor/Driving	390K	A	1.3%
MidAir[19]	Outdoor/In-the-wild	423K	A	4.0%
MVS-Synth[27]	Outdoor/Driving	12K	A	1.2%
Spring[36]	In-the-wild	5K	A	0.7%
Structured3D[74]	Indoor	77K	A	4.8%
Synthia[46]	Outdoor/Driving	96K	A	1.2%
TartanAir[58]	In-the-wild	306K	A	5.0%
UrbanSyn[25]	Outdoor/Driving	7K	A	2.1%
ObjaverseV1[12]	Object	167K	A	4.8%

Table 6. A table of datasets used for training. #Frames stands for the number of used frames. The types are in short for A. synthetic, B. structure from motion / multiview reconstruction, C. LiDAR / Laser; D. Microsoft Kinect

B.2. Evaluation data

The raw evaluation datasets are processed accordingly for reliable evaluation and fair comparison. We report the details as follows.

- **NYUv2** [38] We use the official test split of 654 samples. Due to the inaccuracy of ground truth values captured by

Kinect V1 near boundaries, we filter and remove boundary regions by a simple edge detection method. Specifically, we set a threshold for the difference between the minimum and maximum depth values within a local window. Depth values beyond 5 meters are excluded because they are unreliable due to the limited sensor range. Additionally, we manually mask out areas with reflective and transparent surfaces, such as mirrors and glass, which cannot be accurately captured by the sensor.

- **KITTI** [51] We utilize the test split of 652 images of Eigen et. al. [18] following previous works. The original resolution of 1242×375 does not match our training aspect ratio (ranging from 1 : 2 to 2 : 1), so we apply a center crop to obtain a 750×375 resolution from the raw images.
- **ETH3D** [49] All 454 images are included. The images are undistorted with the official calibration data and downsized from the original 6202×4135 resolution to 2048×1365 .
- **iBims-1** [31] All 100 images are included at an original resolution of 640×480 .
- **GSO** [16] The dataset contains 1,030 objects. For each object, we render a single view at 512×512 resolution. The view is randomly sampled with a FoV ranging from 30° to 60° . The object is centered in the image, and its bounding box occupies approximately 70% of the image’s size.
- **Sintel** [9] We use all 1,064 frames and perform a center crop to 872×436 from the original 1024×436 resolution to fit our aspect ratio range. The sky regions are manually masked out.
- **DDAD** [24] We randomly select 1,000 samples from the validation set. The dataset was collected using multiple cameras and LiDAR sensors mounted on a moving vehicle. Some cameras inadvertently capture parts of the vehicle, causing discrepancies with the sensor’s depth data. To address this, we crop the regions that are not obstructed by the vehicle itself.
- **DIODE** [52] We utilize the official validation split, which includes 325 indoor images and 446 outdoor images at an original resolution of 1024×768 . Due to artifacts in ground truth depth values near the boundaries in this dataset, we identify and remove these boundary regions using a similar approach as described above.

C. More results

C.1. Full table of depth estimation results

In Table 7, we present a full table of results for depth estimation where methods that predict metric or scale-invariant depth are evaluated for affine-invariant depth and disparity for fair comparison with other baselines.

Method	NYUv2		KITTI		ETH3D		iBims-1		GSO		Sintel		DDAD		DIODE		Average		
	Rel ^d _↓	δ_1^d _↑	Rel. _↓	δ_1^d _↑	Rel ^d _↓	δ_1^d _↑	Rel. _↓	δ_1^d _↑	Rel ^d _↓	δ_1^d _↑	Rank _↓								
Scale-invariant depth																			
LeReS	12.1	82.5	19.3	64.3	14.2	78.4	14.0	78.8	13.6	77.9	30.5	52.1	26.5	52.1	18.1	69.9	18.5	69.5	7.31
ZoeDepth	5.65	96.3	7.23	92.2	10.4	87.3	7.48	93.2	3.23	99.9	27.4	61.7	17.0	73.0	11.2	85.4	11.2	86.1	5.50
DUSt3R	4.43	97.1	7.71	90.9	6.07	95.6	4.96	95.9	3.27	99.5	31.1	57.2	18.5	73.5	8.84	88.8	10.6	87.3	5.00
Metric3D V2	4.74	97.3	3.96	98.6	3.92	98.5	4.20	97.7	2.47	99.9	20.7	70.0	7.36	94.6	3.27	98.5	6.32	94.4	2.07
UniDepth	<u>3.88</u>	98.3	3.73	98.7	5.68	97.0	4.76	97.4	4.17	99.7	28.3	58.9	<u>9.98</u>	<u>90.7</u>	6.79	92.9	<u>8.41</u>	<u>91.7</u>	3.00
DA V1*	4.81	97.5	5.52	95.8	8.80	92.3	5.54	95.8	5.48	99.2	28.1	56.7	13.1	81.7	10.1	87.8	10.2	88.4	5.67
- metric indoor	4.81	97.5	15.2	74.2	9.42	89.0	5.54	95.8	5.48	99.2	28.3	56.7	24.2	57.5	10.1	87.8	12.9	82.2	-
- metric outdoor	16.0	72.2	5.52	95.8	8.80	92.3	13.8	78.8	8.60	93.6	28.1	54.8	13.1	81.7	12.9	81.7	13.3	81.4	-
DA V2*	5.09	97.2	7.28	93.6	6.14	95.5	4.33	97.9	4.40	99.3	22.9	65.3	14.6	78.2	7.89	90.3	9.08	89.7	4.06
- metric indoor	5.09	97.2	7.49	91.3	6.14	95.5	4.33	97.9	4.40	99.3	22.9	65.3	16.5	73.6	7.89	90.3	9.35	88.8	-
- metric outdoor	15.3	72.1	7.28	93.6	9.33	89.6	10.6	84.9	9.61	92.5	28.6	57.4	14.6	78.2	12.1	83.6	13.4	81.5	-
Ours	3.48	98.4	4.27	97.8	3.38	98.9	3.45	97.1	1.49	100	19.4	73.4	9.11	90.6	<u>4.85</u>	<u>94.8</u>	6.17	93.9	1.62
Affine-invariant depth																			
LeReS	6.25	95.4	8.15	90.6	8.98	90.7	6.71	94.6	4.03	99.4	24.0	64.8	16.1	75.9	9.93	88.4	10.5	87.5	8.81
ZoeDepth	4.79	97.2	5.51	95.3	7.29	94.2	5.88	95.7	2.54	99.9	21.8	69.2	14.1	80.3	7.72	91.0	8.70	90.3	7.25
DUSt3R	3.76	97.8	7.21	91.8	4.96	96.4	3.92	96.6	2.56	99.6	25.4	64.1	16.8	76.4	6.55	92.9	8.89	89.5	6.69
Metric3D V2	4.00	97.6	3.48	98.5	<u>3.54</u>	<u>98.4</u>	<u>3.25</u>	98.3	2.12	99.4	24.4	71.6	<u>7.10</u>	<u>94.8</u>	2.73	98.8	6.33	94.7	3.50
UniDepth	<u>3.42</u>	98.6	<u>3.54</u>	98.8	4.93	97.5	3.74	98.2	2.47	99.9	24.8	64.1	<u>9.36</u>	<u>91.0</u>	4.88	96.2	<u>7.14</u>	<u>93.0</u>	3.62
Marigold	4.63	97.3	7.29	93.8	6.08	96.3	4.35	97.2	2.78	99.9	21.2	75.0	14.6	80.5	6.34	94.3	8.41	91.8	5.81
GeoWizard*	4.69	97.4	8.14	92.5	6.90	94.0	4.50	97.1	2.00	99.9	17.8	76.2	16.5	75.7	7.03	92.7	8.44	90.7	6.56
- indoor	4.69	97.4	8.14	92.5	6.90	93.9	4.50	97.1	2.00	99.9	17.8	76.0	16.5	75.7	7.03	92.7	8.44	90.7	-
- outdoor	4.83	97.3	8.40	92.2	7.18	93.7	4.59	97.0	2.03	99.9	17.8	76.2	17.1	74.4	7.22	92.5	8.64	90.4	-
- object	4.70	97.4	8.21	92.4	6.92	94.0	4.52	97.0	2.05	99.9	17.9	76.0	16.8	75.1	7.13	92.6	8.52	90.5	-
DA V1*	<u>3.86</u>	98.3	<u>4.94</u>	<u>96.6</u>	6.26	96.5	4.24	97.3	1.98	100	20.1	71.8	11.2	86.2	6.50	93.4	<u>7.55</u>	<u>92.8</u>	4.50
- metric indoor	3.86	98.3	9.78	87.2	6.35	95.0	4.24	97.3	1.98	100	20.1	71.8	16.9	74.2	6.50	93.0	8.72	89.6	-
- metric outdoor	7.72	93.8	4.94	96.6	6.26	96.5	7.01	94.2	2.78	99.8	20.7	70.0	11.2	86.2	6.93	93.4	8.44	91.3	-
DA V2*	4.22	97.8	6.81	94.2	4.66	97.2	3.45	98.3	<u>1.45</u>	100	<u>17.2</u>	<u>76.5</u>	14.2	82.0	5.32	94.9	7.16	92.6	<u>3.19</u>
- metric indoor	4.22	97.8	6.95	92.7	4.66	97.2	3.45	98.3	1.45	100	17.2	76.5	14.2	80.0	5.32	94.9	7.18	92.2	-
- metric outdoor	8.69	90.9	6.81	94.2	7.26	93.5	6.81	93.5	2.28	100	22.5	67.0	13.2	82.0	8.00	91.2	9.45	89.0	-
Ours	2.97	98.6	3.95	98.0	2.71	99.2	2.73	97.9	0.96	100	13.1	83.1	8.33	92.2	<u>3.13</u>	<u>97.6</u>	4.73	95.8	1.56
Affine-invariant disparity																			
LeReS	7.33	95.4	12.4	86.7	10.2	90.1	8.45	92.9	4.33	99.7	28.9	59.6	23.3	73.1	10.8	88.3	13.2	85.7	8.25
ZoeDepth	5.24	97.7	5.86	95.6	8.08	94.0	6.22	96.1	2.59	99.9	26.9	66.3	14.0	81.8	8.17	92.0	9.63	90.4	6.75
DUSt3R	4.27	98.1	7.67	92.2	5.60	96.2	4.47	96.7	2.64	99.8	39.9	56.8	17.4	76.3	7.09	92.8	11.1	88.6	6.75
Metric3D V2	13.4	81.4	<u>3.69</u>	<u>98.3</u>	<u>4.38</u>	<u>97.6</u>	8.56	92.3	1.81	100	21.8	72.5	7.32	94.2	7.62	90.4	8.57	90.8	5.29
UniDepth	<u>3.80</u>	98.7	3.64	98.7	5.34	97.2	4.04	<u>98.1</u>	2.55	99.9	28.5	60.9	<u>9.83</u>	<u>89.3</u>	5.94	95.5	7.96	92.3	3.62
MiDaS V3.1	4.62	98.1	6.30	94.8	5.80	96.8	4.75	97.4	1.88	100	21.4	73.0	14.4	82.7	6.06	94.9	8.15	92.2	5.00
DA V1	4.24	98.4	5.40	97.0	4.70	<u>98.2</u>	4.20	97.6	1.54	100	<u>20.4</u>	<u>77.5</u>	12.6	87.0	5.72	95.7	<u>7.36</u>	<u>93.9</u>	<u>3.00</u>
DA V2	4.20	98.2	5.61	96.8	4.73	<u>98.0</u>	<u>3.48</u>	98.5	<u>1.25</u>	100	21.4	72.8	13.0	86.6	<u>5.33</u>	<u>96.1</u>	7.38	93.4	3.06
Ours	3.41	<u>98.6</u>	4.08	98.1	3.17	98.8	3.20	<u>98.1</u>	0.944	100	18.4	79.5	8.91	91.5	4.00	97.3	5.76	95.2	1.38

Table 7. Full table of comparison for depth map estimation. * Methods have multiple model versions available for respective benchmarks, among which the best for each benchmark is chosen for ranking, followed by the detailed results in smaller text size for each version. Gray numbers denote models trained on respective benchmarks.

C.2. Qualitative comparison on uncurated in-the-wild images

We further utilize the first 100 in-the-wild images in DIV2K[2] dataset to extensively compare our method with LeReS [69], UniDepth [41], DUSt3R [57], Metric3D V2 [26] and Depth Anything V2 [66]. The results can be found in the supplementary videos. Since Metric3D V2 and Depth Anything V2 predict depth map and require ground truth camera focal to obtain 3D points cloud results, we visualize them using our estimated focal lengths.

C.3. More visual results

In the following pages, we demonstrate more examples of our results for in-the-wild images. The rows from left to right are the input images, the disparity maps, surface geometry visualization from the source view and three novel view image of the point cloud, respectively.

